Available online at www.sciencedirect.com
SCIENCE DIRECT®
Surface Science 563 (2004) 191–198
SURFACE SCIENCE
www.elsevier.com/locate/susc

The effective mass of a free-electron-like surface state of the Si(1 1 1)$\sqrt{3} \times \sqrt{3}$-Ag surface investigated by photoemission and scanning tunneling spectroscopies

Toru Hirahara *, Iwao Matsuda *, Masashi Ueno, Shuji Hasegawa

Department of Physics, School of Science, University of Tokyo, 7-3-1 Hongo, Bunkyo-ku, Tokyo 113-0033, Japan

Received in revised form 9 June 2004; accepted for publication 14 June 2004
Available online 21 June 2004

Abstract

A small electron pocket composed of a metallic and parabolic surface-state band of Si(1 1 1)$\sqrt{3} \times \sqrt{3}$-Ag was investigated in detail by high-resolution angle-resolved photoemission spectroscopy (ARPES) and scanning tunneling spectroscopy (STS). The Fermi surface was a complete circle (Fermi ring), and the band dispersion was determined three dimensionally in energy–momentum space. The effective mass (m^*) was extracted by a new method, two-dimensional (2D) fitting to the band dispersion, and compared with the results of conventional analyses of energy and momentum distribution curves (EDC and MDC). The EDC (MDC) analysis gave a m^* value larger (smaller) than that obtained by the 2D fitting method by about 20%. The m^* obtained by the 2D fitting was in good agreement with the value obtained by the STS measurements of electron standing waves, giving the most plausible value of $m^* = (0.13 \pm 0.03)m_e$ (m_e is the free-electron mass) for the parabolic band.

Keywords: Angle resolved photoemission; Scanning tunneling spectroscopies; Surface electronic phenomena (work function, surface potential, surface states, etc.); Silicon; Silver; Metallic surfaces

1. Introduction

Surface superstructures composed of a metallic monolayer on semiconductor surfaces are interesting systems for studying electronic transport phenomena on atomic scale, because their electronic states are located within the energy band gap of the substrate bulk so that the carriers through the surface states are not scattered into the bulk states. These systems are therefore useful to mimic nanometer-scale device structures as well as to explore nano-scale transport physics.

Within the frame of Boltzmann picture, in general, the conductivity tensor of materials in two dimension (2D) is given by [1]:

$$\sigma_{ij} = \frac{1}{2\pi^2}\frac{e^2}{\hbar}\int \tau_k \frac{v_{ki}v_{kj}\,\mathrm{d}k_F}{|v_k|}, \quad (1)$$

where τ_k, k_F and $v_{ki} = \frac{1}{\hbar}\frac{\partial E(k)}{\partial k_i}$ are the carrier relaxation time, Fermi wavevector, and Fermi velocity along the i direction at the Fermi level,

* Corresponding authors. Tel./fax: +81-3-5841-4209.
E-mail addresses: hirahara@surface.phys.s.u-tokyo.ac.jp (T. Hirahara), matsuda@surface.phys.s.u-tokyo.ac.jp (I. Matsuda).

0039-6028/$ - see front matter © 2004 Elsevier B.V. All rights reserved.
doi:10.1016/j.susc.2004.06.157

respectively. The integral is done on the Fermi surface. In a system with an isotropic Fermi surface, Eq. (1) is reduced to the Drude formula:

$$\sigma = \frac{ne^2\tau}{m^*}. \tag{2}$$

The important parameters here are n, τ, and m^*. The carrier density n and the effective mass m^* are directly derived from the band structure at the Fermi level (i.e. Fermi surface); $m^* = \hbar^2\{\frac{\partial^2 E(k)}{\partial k^2}\}^{-1}$. In this way, the electronic band structure near the Fermi level is essential for determining the transport property. The relaxation time τ is a quantity not determined from the band structure, but rather governed by carrier scattering from defects/impurities and phonons.

Band structures of surface states can be directly measured by angle-resolved photoemission spectroscopy (ARPES) with the use of vacuum ultraviolet (VUV) because of the short mean free path of electrons, giving n and m^* values. ARPES measurements with temperature variation, furthermore, provide quantitative information on electron–phonon coupling which is closely related to τ [2]. Thus, ARPES measurements are very useful for interpretations of surface-state transport phenomena.

The Si(1 1 1)$\sqrt{3}\times\sqrt{3}$-Ag surface, which is formed by one monolayer (ML) Ag deposition on a Si(1 1 1) surface (1 ML $= 7.83\times10^{14}$ (atoms/cm^2)), has recently attracted considerable attention, because it is reported to show high-surface conductivity due to the surface-state band [3,4]. In order to interpret the surface conductivity, a large number of ARPES studies have already been done [5–11], which have revealed that a parabolic surface-state band near the Fermi level (S_1 band) plays a central role for the surface transport. The parabolic S_1 band shifts down in energy position below the Fermi level and is partially occupied by electrons (an electron pocket) when a small amount of additional Ag adatoms are deposited on top of the $\sqrt{3}\times\sqrt{3}$-Ag surface. This is due to electron doping into the S_1 band from the adatoms, which causes an increase in surface conductivity [7]. However, by annealing the surface at high temperatures (>600 °C) which removes the adatoms, the S_1 band shifts up above Fermi level [12,13], resulting in the removal of the electron pocket. This is an important phenomenon indicating that the surface conductivity can be controlled by the amount of adatoms on top of it through carrier doping into the surface-state band. The band occupation directly provides the value of n in Eq. (2).

There still remains, however, an issue to be clarified about the electron pocket, i.e., the effective mass. There is a large discrepancy in the m^* value among the previous ARPES reports. Ref. [8] reported $m^* = 0.25$ in the unit of free-electron mass (m_e), while Ref. [14] reported $m^* = 0.07m_e$, which is approximately $\frac{1}{3}\sim\frac{1}{4}$ of the former value. This discrepancy is serious because it causes a large ambiguity in Eq. (2). These two reports have used different methods to extract the m^* value from ARPES data; an analysis of energy distribution curves (EDC) was employed in Ref. [8], while momentum distribution curves (MDC) were analyzed in Ref. [14]. Therefore in the present study, we have done both analyses of our own ARPES data, and compared them with a new method, 2D fitting to the energy–momentum dispersion curves $E(\vec{k}_{\parallel})$. Furthermore, we have also done systematic measurements of electron standing waves on this surface by scanning tunneling spectroscopy (STS), which also provides the energy–momentum dispersion curve through the tip-bias dependence. The m^* value thus obtained agreed well with that obtained by the 2D fitting method in ARPES. It turned out that the EDC (MDC) analysis tends to give a larger (smaller) value than that obtained from the 2D fitting method by about 20%.

Through these comprehensive measurements and analyses, we have concluded that $m^*/m_e = 0.13\pm0.03$ as the most plausible value for the parabolic S_1 band, and the 2D fitting method for ARPES data is more reliable than the EDC or MDC analyses.

2. Experiment

ARPES experiments were performed with a hemispherical photoelectron spectrometer in ultrahigh vacuum, equipped with angle and energy multidetections (Gammadata Scienta SES-100),

using unpolarized HeIα (21.2 eV) radiation. The angle between incident photons and emitted electrons was set to be 50°. The electron energy resolution was ~35 meV and the angular resolution was set ~0.2° in the multidetection angle range of ±3° (better than 1° within the whole angle range of ±6°). Whereas only one spectrum is obtained in the conventional ARPES, with the use of this analyzer, 127 spectra are obtained at once as the raw data which make up a band dispersion image like the one in the left hand side of Fig. 1(a). APRES results shown in the present paper were taken at RT.

STS experiments together with scanning tunneling microscope (STM) observations were done with a commercial ultrahigh vacuum low-temperature STM (UNISOKU USM501 type) at ~65 K [15], using an electrochemically etched tungsten tip. Spectroscopic dI/dV images in STS mode were acquired by lock-in detection technique using tip-bias modulation of ±75 meV with 777 Hz frequency.

An n-type(P-doped) Si(1 1 1) wafer with nominal resistivity of 2–15 Ω cm at RT was used in the experiments. The Si(1 1 1)7×7 surface was prepared by stepwise degassing and finally by flash heating at 1500 K. The Si(1 1 1)$\sqrt{3}\times\sqrt{3}$-Ag surface structure was formed by 1 ML Ag deposition onto the 7×7 surface held at ~520 °C. Ag was deposited using an alumina-coated W basket (in

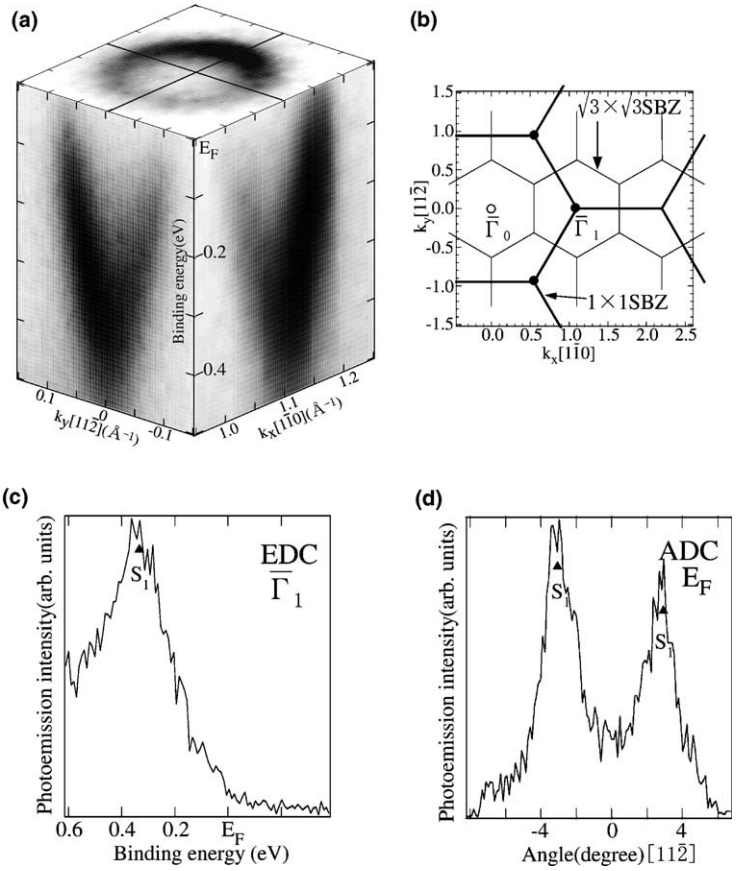

Fig. 1. (a) The Fermi surface and gray-scale band dispersion images in two directions ([11$\bar{2}$] and [1$\bar{1}$0]), measured at RT around the center of the 2nd $\sqrt{3}\times\sqrt{3}$-surface Brillouin zone ($\bar{\Gamma}_1$ point). (b) 1×1 (thick solid lines) and $\sqrt{3}\times\sqrt{3}$ (thin solid lines) surface Brillouin zones. (c) An energy distribution curve(EDC) at the $\bar{\Gamma}_1$ point ($k_y = 0$) of the left hand side band dispersion image of (a). (d) An angular distribution curve (ADC) at the Fermi level of the left hand side band dispersion image of (a).

the STM apparatus) or a graphite effusion cell (in the ARPES system). The quality and cleanliness of the surface were checked with reflection high-energy electron diffraction patterns, ARPES and STM measurements.

3. Results and discussion

An energy contour at the Fermi level and gray-scale band dispersion diagrams of the Si(1 1 1)$\sqrt{3}\times\sqrt{3}$-Ag surface are shown in Fig. 1(a). The band dispersion images were taken along two crystal orientations ([1 1 $\bar{2}$] and [1 $\bar{1}$ 0]) around the $\bar{\Gamma}_1$ point ($k_x = 1.09, k_y = 0$) in the 2nd $\sqrt{3}\times\sqrt{3}$-surface Brillouin zone (SBZ) (see Fig. 1(b)). In this diagram, the intensities of the spectral features are represented by the darkness in the gray scale. The Fermi surface of the S_1 band is a complete circle (Fermi ring) centered at the $\bar{\Gamma}_1$ point. The band dispersion curves in two directions are parabolic and cross the Fermi level. It is clear, thus, that the S_1 band is an isotropic and metallic two-dimensional free-electron like state.

In order to obtain an effective mass of the band, the EDCs or ADCs (angular distribution curves, corresponding to MDCs), are conventionally extracted from the band dispersion diagrams like Fig. 1(a). An EDC is a slice at a certain angle (momentum, or wave vector) in the band dispersion diagram, while an ADC is a slice at a certain energy. An EDC at the $\bar{\Gamma}_1$ point ($k_y = 0$) and an ADC at the Fermi level of the left-side band dispersion image ([1 1 $\bar{2}$] direction) in Fig. 1(a) are depicted in Fig. 1(c) and (d), respectively. The EDCs were obtained in 0.12° steps, and the energy step for the ADCs was 0.01 eV. A single peak is observed in the EDC, which corresponds to the bottom of the parabolic band, while there are two peaks in the ADC, corresponding to two Fermi-level crossings of the band.

The peak energy positions in the EDCs were determined by making a curve-fit with a Lorentzian and integrating background as the EDC can be expressed by a spectral function and its peak width mainly reflects the photohole lifetime [16,17]. A series of EDCs from Fig. 1(a) are shown in Fig. 2(a) with the fitted curves. The Lorentzian line widths were ~160 meV. Relations between the obtained energy positions and the wave vectors are plotted in Fig. 2(b). This is a band dispersion determined from the EDC analysis. The solid line in Fig. 2(b) is a parabola fitted to the experimental data. One can find that the band has parabolic dispersion near the bottom, but shows a deviation from it near the Fermi level (binding energy = 0), which is due to the Fermi–Dirac distribution function of electrons in EDC and a finite energy resolution in the measurements; the peak positions are apparently shifted away from the Fermi level due to the slope of the Fermi–Dirac distribution function. As shown in Fig. 2(c) for the ADCs, the angles (and therefore wavenumbers) at peak positions were determined by making a curve-fit with a Gaussian because the line width is determined by the total angular resolution. Relations between the obtained wavenumbers and energy were plotted in Fig. 2(d). This is a band dispersion determined from the ADC analysis. Data points at binding energy larger than 0.3 eV are missing since the ARPES peaks in (c) are not clearly resolved in this region.

The dispersion curves from the EDC and ADC, shown in Fig. 2(b) and (d), are then fitted with a parabola $E = \frac{\hbar^2 k^2}{2m^*} + E_0$ for EDC (from $k = -0.074$ to 0.074 Å^{-1}) and $k = \pm\frac{\sqrt{2m^*(E-E_0)}}{\hbar}$ for ADC (for $E < 0.29$ eV), where $\hbar$ is Planck's constant divided by 2π and E_0 is the energy at the $\bar{\Gamma}_1$ point. Through these fittings, we have obtained the effective mass m^*, E_0, and the Fermi wavenumber k_F, as summarized in Table 1. While the values of E_0 and k_F are similar between the two methods, m^* derived from EDC is larger than that from ADC by about 50%. One may imagine that this difference comes from the difference in energy region for the fittings; the EDC is fitted near the band bottom, while the ADC is fitted near the Fermi level. But, this is not the case. We did the fitting for both curves in the same energy region (0.13–0.28 eV below Fermi level), which also gave the similar difference in m^* between the two curves. Therefore, the difference is intrinsic in the analysis methods, not a result of non-parabolicity of the band.

For comparison, the resulting dispersion curves are overlapped on the experimental results as

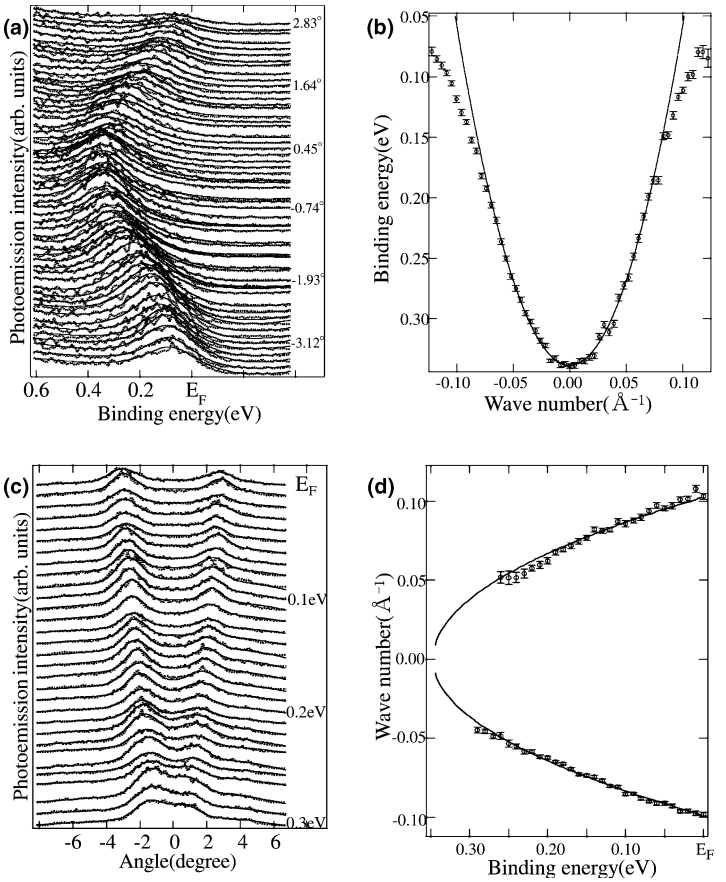

Fig. 2. (a) EDC stacks, taken at 0.12° steps. Dashed lines are raw data, and solid lines are the fitted curves by Lorentzian with integrating backgrounds. (b) Band dispersion using the peak positions determined by the fitting for the EDCs in (a). (c) ADC stacks, taken at 0.01 eV steps. Dashed lines are raw data, and solid lines are the fitted curve by two Gaussians. (d) Band dispersion using the peak positions determined by the fitting for the ADC in (c).

Table 1
The values of m^*/m_e, E_0, k_F for analyses done by EDC, ADC, 2D fit, EDC corrected by the Fermi–Dirac distribution function, and STS

	m^*/m_e	E_0 (eV)	k_F (Å^{-1})
EDC	0.16 ± 0.02	0.32 ± 0.03	0.11 ± 0.01
ADC	0.10 ± 0.03	0.32 ± 0.03	0.10 ± 0.01
2-D	0.12 ± 0.02	0.33 ± 0.03	0.10 ± 0.01
EDC(FD)	0.15 ± 0.02	0.31 ± 0.03	0.11 ± 0.01
STS	0.13 ± 0.03		
Ref. [8] (EDC)	0.25	0.18	0.11
Ref. [14] (MDC)	0.07	0.32	0.08
Ref. [15] (STM)	0.13 ± 0.04		

Values reported by previous researches are also listed.

shown in Fig. 3. We can find that dispersion curves determined from the EDC and ADC analyses locate in the middle of the photoemission intensity distribution in the fitted E–k regions respectively, but they show a slight deviation from each other in the extrapolated regions. It is now clear that band dispersions extracted from the EDC and ADC (MDC) of ARPES results are not identical. This is due to finite resolutions in k and E in the photoemission intensity distribution and inappropriate slicing of the E–k band dispersion map; slicing of such a broad curve at a certain energy or angle do not give precise peak positions.

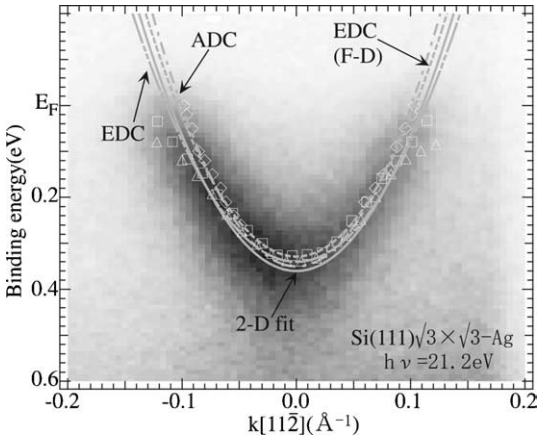

Fig. 3. Peak positions and fitting curves of EDC (△), ADC (◇), EDC with the Fermi–Dirac function correction (□), and the curve fitted two dimensionally, displayed on the gray-scale dispersion image.

In Fig. 3, we have also put energy positions obtained by fitting EDC with Lorentzian and integrating backgrounds including correction by the Fermi–Dirac distribution functions at each angle. The analysis is expected to reduce the influence of the Fermi–Dirac distribution function in EDC that has been described above and to derive the accurate binding energies near the Fermi level [18,19]. The fitted peaks are in more reasonable positions than those without considering the Fermi–Dirac function. The values of m^* and k_F, however, do not differ much from those without correction by the Fermi–Dirac function. This is probably because the bottom of the band is dominant in the curve fitting. Furthermore, the Fermi wavenumber (k_F) obtained by the symmetry method [20], in which the influence of the Fermi–Dirac distribution function is also excluded, gave the same values as those in Table 1.

Next, we have performed a 2D parabolic fit to the E–k band dispersion diagram with chi-square defined as

$$\chi^2 = \sum_i \left(\frac{E(k_i) - E_i}{w_i} \right)^2, \tag{3}$$

where $E(k_i)$ is a fitted value for a given k_i ($E(k_i) = \frac{\hbar^2 k_i^2}{2m^*} + E_0$), and E_i is the experimental data for k_i. A weight parameter, w_i, is an inverse standard deviation of a fit, making intense (k_i, E_i) points in the image of dispersion curve give larger contributions in the curve-fitting. This process looks for the ridge in the 2D (E–k) distribution of the intensity like the one in Fig. 3, and fits a parabola to the ridge two dimensionally. In this procedure, first, we normalized the band dispersion image by each ADC. This is to equalize the intensity distribution for all energies. This procedure is necessary because, in the raw data, the peaks near the Fermi level are weaker in intensity than those in higher binding energy regions [19]. Next we limit the data points used in the fitting. In the case of Fig. 3, the data points in a region of $-0.12 < k_i < 0.12$ Å^{-1} and 0.5 eV$< E_i < E_F$ were used for the 2D fitting. Then we started the fitting procedure, minimizing χ^2, and excluded weak-intensity points from the fitting until the fitted curve became reasonable with the raw data and the fitting parameters did not change much even if we excluded more points. In the summation of Eq. (3), much more points are included than those in the EDC or ADC fitting, which means that the 2D fit reflects the raw data more faithfully than the conventional procedures. The resulting dispersion curve is given in Fig. 3, showing good agreement with the band diagram image in the whole range. The parameters obtained by the 2D fit are listed in Table 1, giving an effective mass in-between those obtained by the conventional EDC and ADC analyses.

Thus it is fairly certain that parabolic dispersion curves and the effective mass are different among the various analysis methods of the same ARPES result. Let us now judge which one is the most reasonable, by comparing them with the results of another technique. It has been well known that electron scattering events lead, through interference, to an oscillatory local density of states (LDOS) or standing waves with a period of a half the wavelength of electrons. Analyses of the LDOS oscillation by STS imaging with different tip bias voltages also provide the energy dispersion of the band [21]. Thus, we investigated such standing waves on the $\sqrt{3} \times \sqrt{3}$-Ag surface by STS experiments. Typical STM and STS (dI/dV) images of the same area on this surface are shown in Fig.

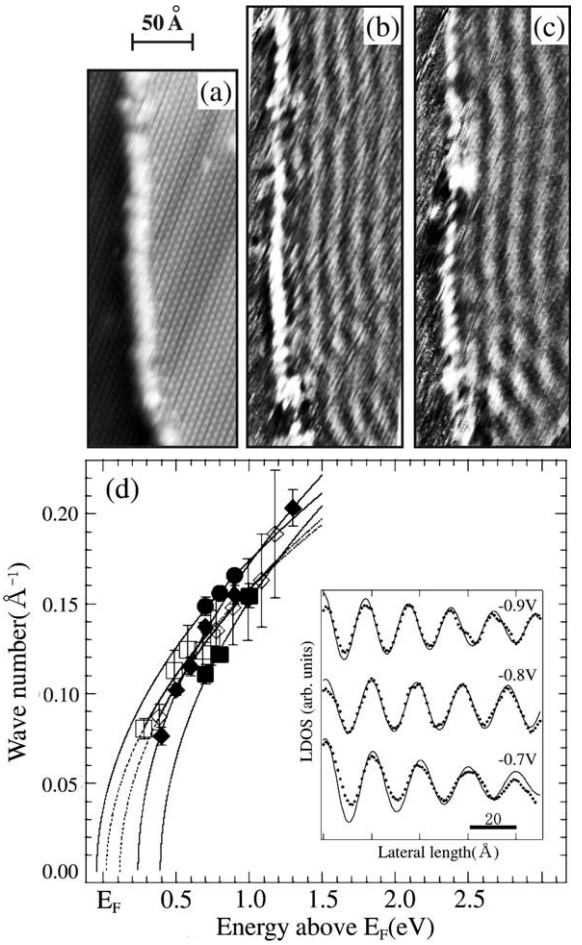

Fig. 4. (a) STM image (in constant current mode) of a Si(1 1 1)$\sqrt{3} \times \sqrt{3}$-Ag near a step at ~65 K with a tip bias $V_T = -0.7V$, tunneling current $I_T = 0.7$ nA. (b),(c): STS images of the same place at (b) $V_T = -0.9$ V, $I_T = 0.7$ nA, and (c) $V_T = -0.7$ V, $I_T = 0.7$ nA. (d) Solid marks are the data obtained from the line profiles of the STS data in the present study, and the solid curves are fitted to them. Open symbols and dashed curves are data from [15]. Inset: Dashed lines are raw data of the line profiles of standing waves for $V_T = -0.7$, -0.8, and -0.9 V. Solid lines are the fit to the raw data with Eq. (4).

4(a) and (b),(c), respectively. One can find, in the STM image, a step edge and flat terraces having the $\sqrt{3} \times \sqrt{3}$-Ag structure, while in the STS images, the standing waves are observed on the terrace near the step edge [15,22]. These standing waves are formed by the electrons in the S_1 band as there are no other bands in this energy region according to the first-principles calculation and inverse photoemission spectroscopy [6,23]. The wave vector (wavelength) of the LDOS oscillation at each tip voltage are obtained through fitting the line profile of the image with

$$\mathrm{LDOS}(x) \propto \exp(-x/l)\cos(2kx - \eta) \tag{4}$$

where x is the distance from the step edge, l is the decay length, k is the wave number, and η is the reflection phase shift. Several results of the line profiles with the fitted curves are shown in an inset of Fig. 4(d). The wave vector (wavelength) clearly varies with tip bias, and thus, a dispersion curve of the surface is obtained. Fig. 4(d) is a summary of the data points acquired by the STS experiments on different surface regions together with those reported in the previous STM observations [15]. By fitting a parabola to each series of data, we obtained an effective mass. The values are similar between the STM and STS results as given in Table 1. However, discrepancies were found for the E_0 values among the curves as shown in Fig. 4(d). This is due to the tip-induced local band bending as reported previously [24–26], which prevents precise determination of an energy position in STM/STS observation on a semiconductor surface at low temperature.

Finally, the m^* values obtained from the various methods in the present and previous researches are compared. The values listed in Table 1 indicate that the effective mass of the S_1 band of the $\sqrt{3} \times \sqrt{3}$-Ag surface is about $0.13m_e$ which are the results of the 2D fitting of ARPES spectra and the STS analysis. The values reported in the previous ARPES studies were larger for EDC [8] or smaller for MDC [14] than the present result of the 2D fitting. The tendency is well reproduced in our EDC and ADC analyses as described above. The difference between the 2D analysis and the EDC/ADC analyses are about 20%. The effective mass obtained by the standing wave analysis is, on the other hand, in good agreement with the 2D fitting. It is now reasonable to conclude that the EDC and MDC analyses raise systematic errors in estimating the effective mass, and that the 2D fitting method is the most appropriate one.

4. Conclusions

We have performed detailed ARPES and STS measurements on the band dispersion and Fermi ring of a metallic surface-state band (S_1 band) of the Si(1 1 1)$\sqrt{3}\times\sqrt{3}$-Ag surface. The effective mass of the band was obtained from the ARPES results with four different procedures of analyzing EDCs, EDCs including a correction of the Fermi–Dirac distribution function, ADC(MDC), and 2D fit. The values were, then, compared to those obtained from the STS observations of electron standing waves. We found that the effective mass is $(0.13\pm0.03)m_e$, which is obtained by the 2D fit of ARPES data and STS measurements. We propose the 2D fitting analysis for obtaining the effective mass of parabolic bands as the most reliable method. Since the effective mass is an important parameter in determining transport phenomena, the present result is expected to play an important role in the interpretation of surface conductivity measurements with sophisticated micro-four-point probes [27,28]. Using the obtained values of $m^* = 0.13m_e$, $n \sim 10^{13}$ cm^{-2} in this experiment and the measured conductivity of $\sigma \sim 10$ μS/□ [29], the relaxation time τ can be estimated to be $\tau \sim 10^{-15}$ s from Eq. (2), which is in the same order of magnitude as that for another metallic surface, Si(1 1 1)4×1–In [1]. The details of the analysis will be reported elsewhere [29].

Acknowledgements

J. Sugawa and T. Kawaguchi are gratefully acknowledged for their helps during the experiments. This work has been supported by Grants-In-Aid from the Japanese Society for the Promotion of Science.

References

[1] T. Kanagawa, R. Hobara, I. Matsuda, T. Tanikawa, A. Natori, S. Hasegawa, Phys. Rev. Lett. 91 (2003) 036805.
[2] M. Hengsberger, R. Frésard, D. Purdie, P. Segovia, Y. Baer, Phys. Rev. B. 60 (1998) 10796.
[3] S. Hasegawa, I. Shiraki, T. Tanikawa, C.L. Petersen, T.M. Hansen, P. Bøggild, F. Grey, J. Phys.: Condens. Matter 14 (2002) 8379.
[4] S. Hasegawa, X. Tong, S. Takeda, N. Sato, T. Nagao, Prog. Surf. Sci. 60 (1999) 89.
[5] L.S.O. Johansson, E. Landemark, C.J. Karlsson, R.I.G. Uhrberg, Phys. Rev. Lett. 63 (1989) 2092; Phys. Rev. Lett. 69 (1992) 2451.
[6] J. Viernow, M. Henzler, W.L. O'Brien, F.K. Men, F.M. Leibsle, D.Y. Petrovykh, J.L. Lin, F.J. Himpsel, Phys. Rev. B 57 (1998) 2321.
[7] Y. Nakajima, S. Takeda, T. Nagao, X. Tong, S. Hasegawa, Phys. Rev. B 56 (1997) 6782.
[8] X. Tong, C.S. Jiang, S. Hasegawa, Phys. Rev. B 57 (1998) 9015.
[9] X. Tong, Y. Sugiura, T. Nagao, T. Takami, S. Takeda, S. Ino, S. Hasegawa, Surf. Sci. 408 (1998) 146.
[10] X. Tong, S. Ohuchi, N. Sato, T. Tanikawa, T. Nagao, I. Matsuda, Y. Aoyagi, S. Hasegawa, Phys. Rev. B 64 (2001) 205316.
[11] T. Hirahara, I. Matsuda, S. Hasegawa, e-J. Surf. Sci. Nanotechnol. 2 (2004) 141.
[12] R.I.G. Uhrberg, H.M. Zhang, T. Balasubramanian, E. Landemark, H.W. Yeom, Phys. Rev. B 65 (2002) 081305.
[13] H.M. Zhang, K. Sakamoto, R.I.G. Uhrberg, Phys. Rev. B 64 (2001) 245421.
[14] J.N. Crain, K.N. Altmann, C. Bromberger, F.J. Himpsel, Phys. Rev. B 66 (2002) 205302.
[15] N. Sato, S. Takeda, T. Nagao, S. Hasegawa, Phys. Rev. B 59 (1999) 2035.
[16] S. Hüfner, Photoelectron Spectroscopy, Springer, 1995.
[17] C.R. Ast, H. Höchst, Phys. Rev. B 66 (2002) 125103.
[18] I. Matsuda, M. Hengsberger, F. Baumberger, T. Greber, H.W. Yeom, J. Osterwalder, Phys. Rev. B 68 (2003) 195319.
[19] T. Greber, T.J. Kreutz, J. Osterwalder, Phys. Rev. Lett. 79 (1997) 4465.
[20] J. Mesot et al., Phys. Rev. B 63 (2001) 224516.
[21] L. Petersen, P.T. Sprunger, Ph. Hofmann, E. Lægsgaard, B.G. Briner, M. Doering, H.P. Rust, A.M. Bradshaw, F. Besenbacher, E.W. Plummer, Phys. Rev. B 57 (1998) R6858.
[22] I. Matsuda , M. Ueno , T. Hirahara , R. Hobara , H. Morikawa , S. Hasegawa, Phys. Rev. Lett., submitted for publication.
[23] H. Aizawa, M. Tsukada, Phys. Rev. B 59 (1999) 10923.
[24] R.M. Feenstra, Phys. Rev. B 60 (1999) 4478.
[25] R.M. Feenstra, G. Meyer, F. Moresco, K.H. Rieder, Phys. Rev. B 64 (2001) 081306.
[26] V. Ramachandran, R.M. Feenstra, Phys. Rev. Lett. 82 (1999) 1000.
[27] S. Hasegawa, F. Grey, Surf. Sci. 500 (2002) 84.
[28] T. Tanikawa, I. Matsuda, R. Hobara, S. Hasegawa, e-J. Surf. Sci. Nanotechnol. 1 (2003) 50.
[29] I. Matsuda et al., in press.